Dalton Transactions

ROYAL SOCIETY OF CHEMISTRY

PAPER

View Article Online
View Journal | View Issue

Check for updates

Cite this: *Dalton Trans.*, 2025, **54**, 3444

Electrochemical and spectroelectrochemical investigation of Ru(por)(NO)(OAr) derivatives (por = octaethylporphyrin, tetraanisolylporphyrin; Ar = Ph, C_6H_4-2-NHC(=O)CF_3; C_6H_3-2,6-(NHC(=O)CF_3)$_2$)†

Anthony R. Ramuglia,[a] Jeremy R. Zink,[b] Adam J. Warhausen,[c] Erwin Abucayon,[b] Nan Xu,[b] Kailash Shrestha,[a] George Richter-Addo *[b] and Michael J. Shaw *[a]

Received 30th September 2024,
Accepted 15th January 2025

DOI: 10.1039/d4dt02764g

rsc.li/dalton

The electrochemistry and spectroelectrochemistry of Ru(porphyrin)(NO)(phenoxide) complexes Ru(por)(NO)(OPh) (por = OEP, **1a**; TAP, **2a**; Ph = C_6H_5), Ru(por)(NO)(OAr^1) (por = OEP, **1b**; TAP, **2b**; OAr^1 = –OC_6H_4-(2-NHC(=O)CF_3)), Ru(por)(NO)(OAr^2) (por = OEP, **1c**; TAP, **2c**; OAr^2 = OC_6H_3-(2,6-NHC(=O)CF_3)$_2$; OEP = octaethylporphyrinato dianion, TAP = tetraanisolylporphyrinato dianion) indicate that initial one-electron oxidation results in structure-dependent net reactivity at the phenoxide ligand. Oxidation of **1a** generates **1a**$^+$, which undergoes a relatively slow rate-limiting second-order follow-up reaction. In contrast, **2a** undergoes a diffusion-limited follow-up reaction after oxidation. Oxidation of species **1b** and **2b** results in dissociation of the corresponding phenoxide radicals from the metal center following a relatively slow first-order kinetic process. The $^{\bullet}$OAr^1 radical was detected by EPR spectroelectrochemistry. The follow-up reactions after oxidation of **1c** and **2c** are also very fast. In all cases, the ultimate fate of the ruthenium complex is to be trapped with adventitious water to generate the stable aqua complex. Further oxidation of each compound at higher potentials occurs at the porphyrin ligand, generating the π-radical cation observed by IR spectroelectrochemistry.

Introduction

Metallo-proteins such as heme catalase, HasAp[1] and IsdB[2] contain a heme cofactor with an aryloxide ligand that is contained in the active site in their enzymatic transformations.[3] The heme catalase enzyme facilitates the disproportionation reaction of H_2O_2 and O_2 to H_2O with exceptionally high catalytic turnover frequencies, helping to protect organisms from destructive reactive oxygen species.[3,4] The active site of heme catalase contains an iron–heme complex bound to the surrounding protein *via* the phenolate head group of a tyrosine residue with hydrogen bonding protons coordinated to the O-atom from neighboring arginine residues.[3]

Diatomic nitric oxide (NO) interacts with the heme macrocycle at the Fe centers, forming Fe–NO derivatives that have significant biological implications. The subject of NO binding to heme derivatives has been reviewed extensively.[5,6] NO has been shown to bind to the iron–heme site and inhibit heme catalase, thereby regulating reactive oxygen species (H_2O_2) levels within cells.[4,7] The physiological function of iron–heme nitrosyls are dependent on their Fe–NO binding interaction, influenced by the trans axial ligand's electron-donating ability into the d_{z^2} orbital of the metal.[8] As such, modulating the electronic donation of the O-ligand is expected to influence the electronics and function of the Fe–NO unit.

Few synthetic analogs of the Fe(por)(NO)(O-ligand) structure have been reported, likely due to their instability in solution.[9] Heavier analogs which contain ruthenium act as valence isoelectronic congeners that are more stable and tend to be diamagnetic. Recently, we have reported the preparation and redox behavior of ruthenium nitrosyl porphyrins with axial bonded O-ligands.[10,11] In the current work, we examine the consequences of electron transfer for a set of Ru(por)(NO)(O-ligand) (por = OEP, TAP; OEP = octaethylporphyrinato dianion; TAP = tetra(*p*-$C_6H_4OCH_3$)porphyrinato dianion) with varied hydrogen bonding characteristics, formulated as Ru(por)(NO)

[a]*Department of Chemistry, Southern Illinois University Edwardsville, Edwardsville, IL, 62025-1652 USA. E-mail: michsha@siue.edu*
[b]*Department of Chemistry and Biochemistry, Stephenson Life Sciences Research Center, University of Oklahoma, 101 Stephenson Parkway, Norman, OK 73019, USA*
[c]*Department of Chemistry, Saginaw Valley State University, 7400 Bay Road, University Center, MI 48710, USA*

†Electronic supplementary information (ESI) available. CCDC 2340852 and 2340853. For ESI and crystallographic data in CIF or other electronic format see DOI: https://doi.org/10.1039/d4dt02764g

(OPh) (OEP, **1a**; TAP, **2a**, Ph = C_6H_5), Ru(por)(NO)(OAr^1) (OEP, **1b**; TAP, **2b**; Ar^1 = –C_6H_4-(2-NHC(=O)CF_3)), Ru(por)(NO)(OAr^2) (OEP, **1c**; TAP, **2c**; Ar^2 = C_6H_3-(2,6-NHC(=O)CF_3)$_2$) shown in Fig. 1. These complexes feature phenoxide ligands based on phenol, *N*-2-hydroxyphenylenetrifluoroacetamide, and *N*,*N*′-(2-hydroxy-1,3-phenylene)bis[trifluoroacetamide]. The latter two phenoxides feature amide substituents which are capable of H-bonding with the O-atom bound to the metal center.[12] The complexes comprise a series where there are 0, 1, and 2 H-bonds present in progressively less electron rich environments as determined by single crystal X-ray diffraction.[12–14]

An initial report of this work[14] described the synthesis and characterization (NMR, IR, ESI-MS, X-ray) of the compounds **1a–1c** and preliminary electrochemistry studies. We have prepared the analogous complexes **2a–2c** for comparisons of their redox chemistry with **1a–1c**. The current report covers in-depth cyclic voltammetry, IR-spectroelectrochemistry, EPR spectroelectrochemistry, and digital simulations to explore the consequences of the oxidation of compounds **1a–1c** and **2a–2c**.

Experimental

All syntheses were performed under an anaerobic (N_2) atmosphere using standard Schlenk glassware and/or in an Innovative Technology Labmaster 100 Drybox. Solutions for spectral studies were also prepared under a nitrogen atmosphere. Dichloromethane, benzene and hexane used in the experiments were dried using an Innovative Technology Inc. Pure Solv 400-5-MD Solvent Purification System. 2-Trifluoroacetylaminophenol,[12,13] 2,6-bis(trifluoroacetylamino)phenol,[12,13] and Ru(TAP)(NO)(O-i-C_5H_{11}) (TAP = tetraanisolylporphyrinato dianion)[15] were synthesized as reported previously. Phenol (≥99%) was obtained from Aldrich and used as received. Chloroform-*d* ($CDCl_3$, 99.96% atom%D) was purchased from Cambridge Isotope Laboratories, deaerated and dried using activated 4 Å molecular sieves. Infrared spectra were recorded on a Bruker Tensor 27 FTIR spectrometer. Proton NMR spectra were obtained on a Varian 400 MHz spectrometer and the signals referenced to the residual signal of the solvent employed ($CHCl_3$ at δ = 7.26 ppm). X-ray diffraction data were collected using a D8 Quest κ-geometry diffractometer with a Bruker Photon II cpad area detector and Mo-K_α source (λ = 0.71073 Å). Details of X-ray crystallography data collection are found in the ESI Experimental section.† ESI Table S1† contains a summary of crystal data and structural refinement.

Ru(TAP)(NO)(OPh) (2a)

To a stirred CH_2Cl_2 (15 mL) solution of Ru(TAP)(NO)(O-i-C_5H_{11}) (50 mg, 0.053 mmol) was added phenol (15 mg, 0.16 mmol). The mixture was stirred for 4 h at room temperature, and the reaction progress was monitored by solution IR spectroscopy (NaCl plates). A new band at 1831 cm^{-1} was formed with concomitant and complete disappearance of the starting ν_{NO} band of Ru(TAP)(NO)(O-i-C_5H_{11}) at 1807 cm^{-1}. The solvent was removed *in vacuo*, the residue re-dissolved in benzene and passed through an alumina column (Activity Grade III). Benzene was used to elute a dark red band that was collected. The solvent of this collected band was removed *in vacuo* and the product obtained in 69% yield (35 mg,

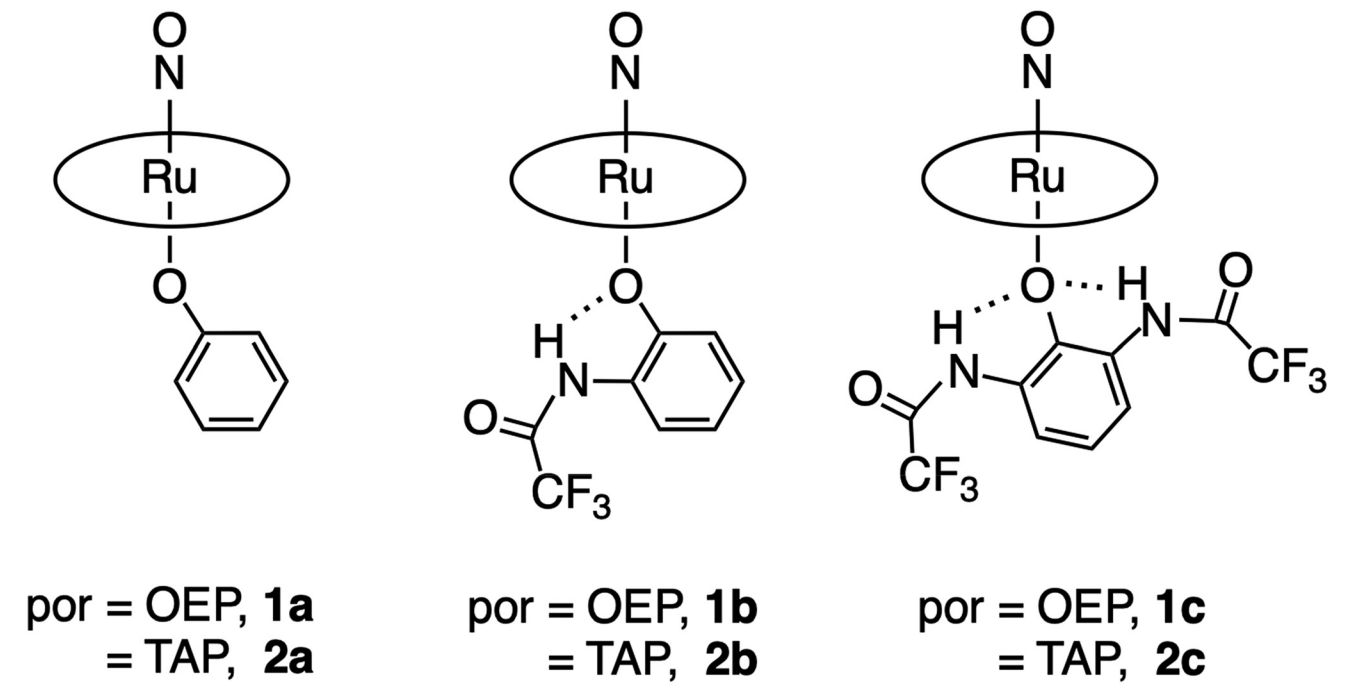

Fig. 1 Synthetic ruthenium metallo-porphyrin complexes investigated in this work.

0.036 mmol). IR (KBr, cm^{-1}): ν_{NO} = 1828. ^1H NMR (400 MHz; $CDCl_3$): δ 8.96 (s, 8H, pyrrole-H of TAP), 8.20 (dd, 4H, *o*-H of TAP, J = 3 and 8 Hz), 8.05 (dd, 4H, *o*′-H of TAP, J = 3 and 8 Hz), 7.31 (app m, 8H, *m*-H of TAP), 5.69 (t, 1H, *p*-H of phenolate moiety, J = 8 Hz), 5.55 (t, 2H, *m*-H of phenolate moiety, J = 8 Hz), 4.12 (s, 12H, *p*-OMe of TAP), 1.51 (d, 2H, *o*-H of phenolate moiety, J = 8 Hz). X-ray diffraction quality crystals were obtained by slow evaporation using layered CH_2Cl_2 and *n*-hexane (1 : 1). IR and NMR data are available in ESI Fig. S1 and S2.† ESI Fig. S3† shows experimental and simulated ^1H spectra of the phenyl region of the ^1H spectrum. A preliminary X-ray crystal structure was consistent with the formulation of the product as Ru(TAP)(NO)(OPh) as derived from IR and ^1H NMR spectral data (ESI Fig. S4†).

Ru(TAP)(NO)(O-*o*-(NHC(=O)CF_3)C_6H_4) (2b)

This compound was prepared similarly as above from Ru(TAP)(NO)(O-i-C_5H_{11}) (50 mg, 0.053 mmol) using 2-trifluoroacetylamino phenol (32 mg, 0.16 mmol). The chromatographed product was obtained in 78% yield (44 mg, 0.041 mmol). IR (KBr, cm^{-1}): ν_{NH} = 3349, ν_{NO} = 1836, ν_{CO} = 1720. ^1H NMR (400 MHz; $CDCl_3$): δ 9.02 (s, 8H, pyrrole-H of TAP), 8.11 (overlapping dd, 8H, *o*-H of TAP, J = 3 and 8 Hz), 7.33 (overlapping dd, 8H, *m*-H of TAP, J = 3 and 8 Hz), 6.72 (d, 1H, *p*-H of phenolate moiety, J = 8 Hz), 5.67 (t, 1H, *m*-H of phenolate moiety, J = 8 Hz), 5.47 (t, 1H, *m*-H of phenolate moiety, J = 8 Hz), 4.12 (s, 12H, *p*-OMe of TAP), 3.37 (br s, 1H, NH of axial ligand), 0.86 (d, 1H, *o*-H of phenolate moiety, J = 8 Hz). IR and NMR data are available in ESI Fig. S1 and S2.† X-ray diffraction quality crystals were obtained by slow evaporation from CH_2Cl_2/*n*-hexane.

Ru(TAP)(NO)(O-2,6-(NHC(=O)CF_3)$_2C_6H_3$) (2c)

This compound was prepared similarly from Ru(TAP)(NO)(O-i-C_5H_{11}) (50 mg, 0.053 mmol) using 2,6-bis(trifluoroacetylamino)phenol (50 mg, 0.16 mmol). The chromatographed product was obtained in 56% yield (35 mg, 0.030 mmol). IR (KBr, cm^{-1}): ν_{NH} = 3339 and 3371, ν_{NO} = 1851, ν_{CO} = 1728. ^1H NMR (400 MHz; $CDCl_3$): δ 9.06 (s, 8H, pyrrole-H of TAP), 8.35 (dd, 4H, *o*-H of TAP, J = 3 and 8 Hz), 7.93 (dd, 4H, *o*-H of TAP, J = 3 and 8 Hz), 7.45 (dd, 4H, *m*-H of TAP, J = 3 and 8 Hz), 6.75 (d, 2H, *m*-H of phenolate moiety, J = 8 Hz), 5.79 (t, 1H, *p*-H of phenolate moiety, J = 8 Hz), 4.13 (s, 12H, *p*-OMe of TAP), 3.17 (br s, 2H, NH of axial ligand). Partial signal overlap was observed between the $CDCl_3$ solvent peak at 7.26 ppm and the *m*-H's of TAP at 7.28 ppm. IR and NMR data are available in ESI Fig. S1 and S2.† X-ray diffraction quality crystals were obtained by slow evaporation from CH_2Cl_2/*n*-hexane (1 : 1).

For electrochemical measurements at SIUE, all chemical manipulations were carried out under an inert atmosphere of nitrogen or argon gas using standard Schlenk glassware and a glove box. Solvents used were pre-dried, distilled and freeze–pump thaw degassed before use. Ferrocene was obtained from Acros Chemicals, and sublimed before use. Compounds **1a–1c** and **2a–2c** were synthesized at the University of Oklahoma. The supporting electrolyte NBu_4PF_6 for electrochemical experiments was obtained from Millipore-Sigma, recrystallized from hot ethanol and dried in a drying pistol at 100 °C for three days. Electrochemical measurements were recorded with a EG&G PAR 263A potentiostat operated *via* a PC and PAR 270 software or through custom LabView software interfaced to the potentiostat *via* a National Instruments USB-6251 A/D board. Measurements were performed in an inert-atmosphere drybox under argon using a 1.6 mm Pt disk as the working electrode, a silver wire pseudo-reference electrode and a platinum wire auxiliary electrode. The potential of ferrocene measured under these conditions was typically 0.35 V *vs.* Ag/AgCl, but was measured independently at the end of each experiment.

IR-spectroelectrochemical measurements were performed using a Bruker Tensor 22 FTIR spectrometer equipped with a mid-IR fiber-optic dip probe with ZnSe waveguide and liquid nitrogen cooled MCT detector available from RemSpec Corporation and an in-house designed cell as described previously.[16] All spectroelectrochemical experiments were conducted under a blanket of argon and performed at 25 °C.

EPR spectra were recorded with a Bruker X-Band EMX^{plus} system at 22 °C. EPR spectroelectrochemical samples were prepared in the drybox under an atmosphere of argon by injecting 2 mL of 0.5 mM **1b**/1 M NBu_4PF_6/CH_2Cl_2 solution into a Wilmad EPR spectroelectrochemistry cell equipped with a silver-wire pseudo reference electrode.

Experimental CV data are plotted as normalized current *vs.* potential plots, after correction for uncompensated resistance (R_u) drop and double layer capacitance (C_{dl}) as described previously.[17] LabView and Python programs were written to implement these transformations. Procedures for iR_u correction in this work,[17] and the limitations of digital iR_u correction[18] have been described previously. Plots of voltammograms are displayed following the IUPAC convention with anodic currents represented as positive. Currents have been converted to the dimensionless form, $\Psi(t)$, through eqn (1),[19,20] where $i(t)$ is the experimental current in amps, F is Faraday's constant, A is the electrode area (measured to be 0.020 cm^2 in these studies), D is the diffusion coefficient (measured as 8.0×10^{-6} cm^2 s^{-1}), C is the concentration of analyte (mol cm^{-3}), ν is the scan rate (V s^{-1}), R is the gas constant 8.31441 J mol^{-1} K^{-1}, and T is the temperature (K).

$$\varphi(t) = \frac{i(t)}{FAC\left(\frac{DF\vartheta}{RT}\right)^{\frac{1}{2}}} \quad (1)$$

Digital simulations and curve fitting were conducted in DigiElch 8F (ElchSoft.com, available from Gamry Instruments). DigiElch simulations were performed with values of R_u and C_{dl} estimated from the behavior of the internal standard ferrocene added at the end of each experiment.

Additional note

CV data can be mathematically transformed to equivalent depictions reminiscent of other techniques.[21] It may be useful

for readers who are less experienced with convolution methods to note that if a function is semi-integrated twice, the result must be the same as regular integration. Commonly, the Riemann–Liouville definition of the semi-integral is used in convolution analysis of CV data.[22] Semi-differentiation is performed by taking the full derivative of the semi-integral. Semi-integration and semi-differentiation of normalized CV data can allow easier access to diagnostic information.[23,24] Thus, if iR_u effects have been compensated or mathematically corrected, semi-integration of a 1-electron Nernstian CV feature results in an S-shaped wave where the forward and reverse current overlap, reminiscent of steady-state voltammetry methods.[23a,25] If diffusion coefficients, concentrations, and electrode areas are known, the height of the plateau allows an estimate of n, the number of equivalents of electrons transferred. The derivative of such plots appear similar to differential pulse voltammograms with heights proportional to n^2.[26] Ryan made effective use of semi-derivative plots in a recent paper on Fe(por)(NO) compounds related to the title species.[27]

Results and discussion

Synthesis and characterization

Complexes **1a–1c** have been reported previously from the reactions of the precursor Ru(OEP)(NO)(O-i-C_5H_{11}) with the respective aryloxides.[14a] The syntheses of complexes **2a–2c** employed similar methodology and were obtained in 56–78% isolated yields (see ESI†). The IR spectra of complexes as KBr pellets revealed bands assigned to ν_{NO} which increase in the order **2a** (1828 cm^{-1}) < **2b** (1836 cm^{-1}) < **2c** (1851 cm^{-1}) reflecting the decreased electron density provided by the more substituted aryloxides (ESI, Fig. S1†). In addition, bands due to ν_{CO} are present for the complexes **2b** and **2c**, consistent with the presence of the amide moieties in the axial aryloxide ligands. Their ^{1}H NMR spectra are consistent with their diamagnetic formulations (Fig. S2†), and the protons of the –C_6H_4OMe-*p* groups of the porphyrin macrocycle display characteristic AA′BB′ splitting patterns (Fig. S3†).[28,29] The X-ray crystal structures of **2b** and **2c** are shown in Fig. 2; see also ESI† for the preliminary X-ray structure of **2a**.

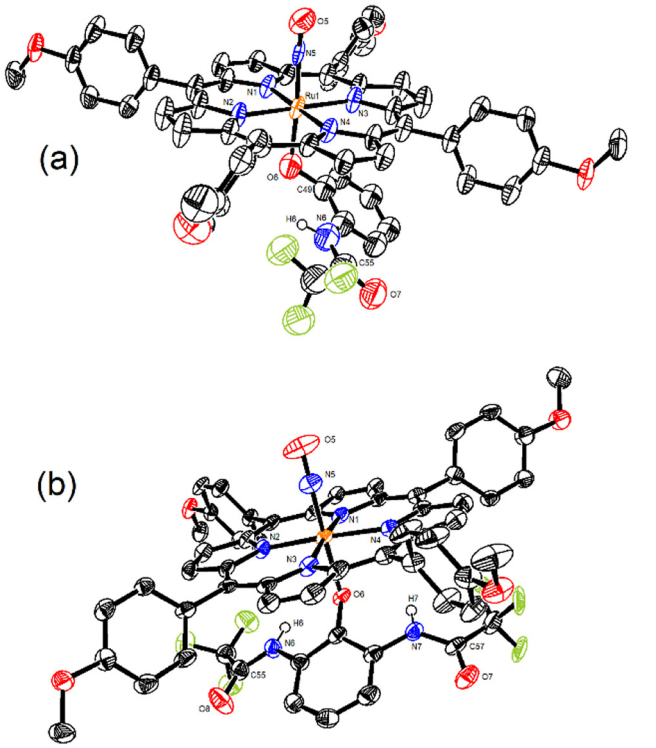

Fig. 2 X-ray crystal structures of (a) **2b**, and (b) **2c**. Hydrogen atoms are omitted for clarity, with the exception of the N6–H6 and N7–H7 hydrogen atoms. Only the major disordered components are shown; details of the structures are shown in the ESI.†

Electrochemistry of OEP species 1a–1c

Fig. 3 depicts iR_u-corrected[18] CV data for the first oxidation of **1a** and **1b** in 0.1 M NBu_4PF_6 at varying scan rates plotted as $\Psi(t)$ *vs.* potential. For compounds **1a** and **1b**, the normalized currents for the forward wave of the first oxidation feature overlap well for different scan rates, and suggest a reversible electron-transfer reaction. In contrast, the first oxidation of **1c** is completely irreversible as shown in ESI Fig. S5.† Each complex displays further oxidations as shown in the semi-derivative plots in Fig. 4 and in the $\Psi(t)$ *vs.* potential plots in ESI Fig. S6.†

The scan-rate dependent reversibility of the 1-electron oxidation for all three compounds is further emphasized by the semi-derivative plots (Fig. 4), where the first oxidation's forward current clearly overlaps for all scan rates, and the peak is 91 mV wide at half-height, consistent with a 1-electron process. Additionally, the re-reduction feature becomes more pronounced as scan rate increases, suggesting that the electron-transfer step is followed by a reaction whose rate is competitive with the scan rate used. For compound **1c**, the oxidation feature's normalized height is approximately constant with scan rate, but the peak potential is scan-rate dependent and the feature appears completely irreversible at all scan rates used. This first oxidation merges at faster scan rates with a subsequent oxidation which occurs at higher potentials (ESI Fig. S10†), but can be distinguished in the semi-derivative plot which clearly shows the progression of the peak potential (approximately $E_{1/2}$) with scan rate (Fig. 4C). The semi-integrated experimental CV data for the forward scan of species **1a–1c** also indicate that the first oxidation of each species involves one electron (ESI Fig. S7†).

Scanning to higher potentials reveals further oxidations for each species. Although the semi-derivative traces for the first oxidation of complex **1a** overlap, two further features whose heights depend on scan rates are present. A wave labelled Y in Fig. 4A at E° = 0.71 *vs.* $Cp_2Fe^{0/+}$ is observable as a small peak at fast scan rates but at slow scan rates it is more prominent as a shoulder on the peak labelled X. Peak Y is assigned as the oxidation of the $[Ru(OEP)(NO)(H_2O)]^+$ cation (*vide infra*), and appears in all CV's for **1a–1c**. The wave labelled X at E° = 0.86 V appears in scans of **1a** and decreases in intensity with

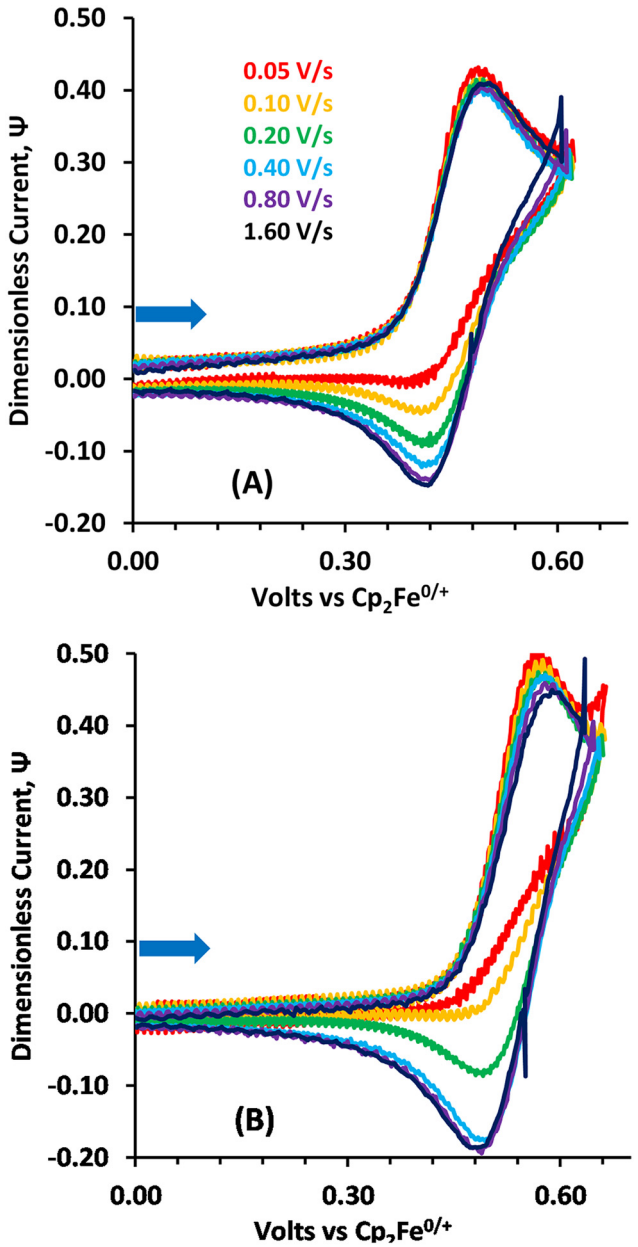

Fig. 3 Ψ *vs.* E representation of R_u- and C_{dl}-corrected CV data collected at 298 K in CH_2Cl_2/0.1 M NBu_4PF_6 with 0.02 cm^2 Pt working electrode, R_u = 1.5 kΩ, C_{dl} = 1.0 μF. (A) 1.1 mM complex **1a** (B) 1.3 mM complex **1b**. Blue arrow indicates initial scan direction.

increasing scan rate. This feature is assigned to products which must subsequently give rise to the aquo complex. As described later, complex **1a** reacts by a second-order process after oxidation in contrast to **1b** (and presumably **1c**), which explains why X is only observed for **1a**. Instead scans of **1b** display a peak labelled Z in Fig. 4B at E° = 0.92 V which increases in intensity with increasing scan rate. This feature is ascribed to the second oxidation of **1b**, *i.e.* the $\mathbf{1b}^{+/2+}$ couple. The $\mathbf{1a}^{+/2+}$ couple appears to be beyond the solvent limit.

Cyclic voltammetry measurements at varying concentrations of **1a** give insight into the consequences of its oxidation. For second-order follow-up reactions, the CV shape should show concentration dependence while no such dependence should be observed for first-order follow-up reactions.[30] This is shown clearly in the semi-derivative plot in Fig. 5 which depicts the oxidation of species **1a** at concentrations of 1.1 mM (top) and 0.27 mM (bottom). The Ψ *vs.* E representation is shown as ESI Fig. S9.† The plots recorded at 0.27 mM display higher reversibility than achieved at 1.1 mM. The improvement in reversibility is consistent with the presence of a second-order rate-limiting chemical step which follows the initial oxidation. The improved reversibility also rules out the effect of adventitious water before the rate-limiting step since the low-concentration data should be more severely affected by the constant amount of adventitious water present in these experiments, as all data was collected with the same batch of solvent and supporting electrolyte in a drybox.

Species **1c** (Fig. 4c) displays an irreversible initial oxidation whose peak potential varies with scan rate. The second oxidation at E° = 0.71 *vs.* $Cp_2Fe^{0/+}$ displays reversibility. This behavior is in agreement with a rapid chemical dissociation event that takes place after the initial oxidation of **1c** to $\mathbf{1c}^+$ which generates a new species that undergoes a subsequent reversible oxidation. This new species is observed for all complexes **1a–1c** at a potential consistent with the presence of the known $[Ru(OEP)(NO)(H_2O)]^+$ complex,[31] likely formed by reaction of the initial electrooxidation product(s) with adventitious water.

A plot of peak potential *vs.* log(ν) for compound **1c** is presented in ESI Fig. S8.† The slope of the line is 37 mV per decade. Diagnostic values of such slopes for irreversible EC reactions according to Saveant[20,32] are 29.6 mV for a concerted EC process or diffusion limited chemical reaction following electron-transfer and 59.2 mV for a slow follow-up chemical reaction at 298 K. The value of 37 mV lies between these two values, indicating that a short-lived intermediate exists in solution as was the case for systems described previously by Amatore for the reduction of metal carbonyl complexes.[33] Under the same conditions, the peak potentials for **1a** and **1b** do not show variation as expected for CV features which show some reversibility. This is consistent with our determination that complex $\mathbf{1c}^+$ must decompose at a rate much faster than either $\mathbf{1a}^+$ or $\mathbf{1b}^+$.[34]

The trend in the observed potentials for the first oxidation for compounds **1a–1c** is consistent with the decrease in electron density expected as electron-withdrawing substituents are placed on the phenoxide ligand (Table 1).

Electrochemistry of TAP species 2a–2c

CV (Ψ *vs.* E), semi-derivative, and semi-integral plots for **2a**, **2b**, and **2c** are given as ESI Fig. S10, S11 and S12,† respectively. As was the case for the octaethylporphyrin species, the semi-integrated experimental CV data for the forward scan of species **2a–2c** indicate that the first oxidation of each species involves one electron (ESI Fig. S12†). The electrochemical data is summarized in Table 1. The TAP complexes are uniformly oxidized at more positive potentials than the OEP species, reflecting the more electron-rich nature of the latter ligand.

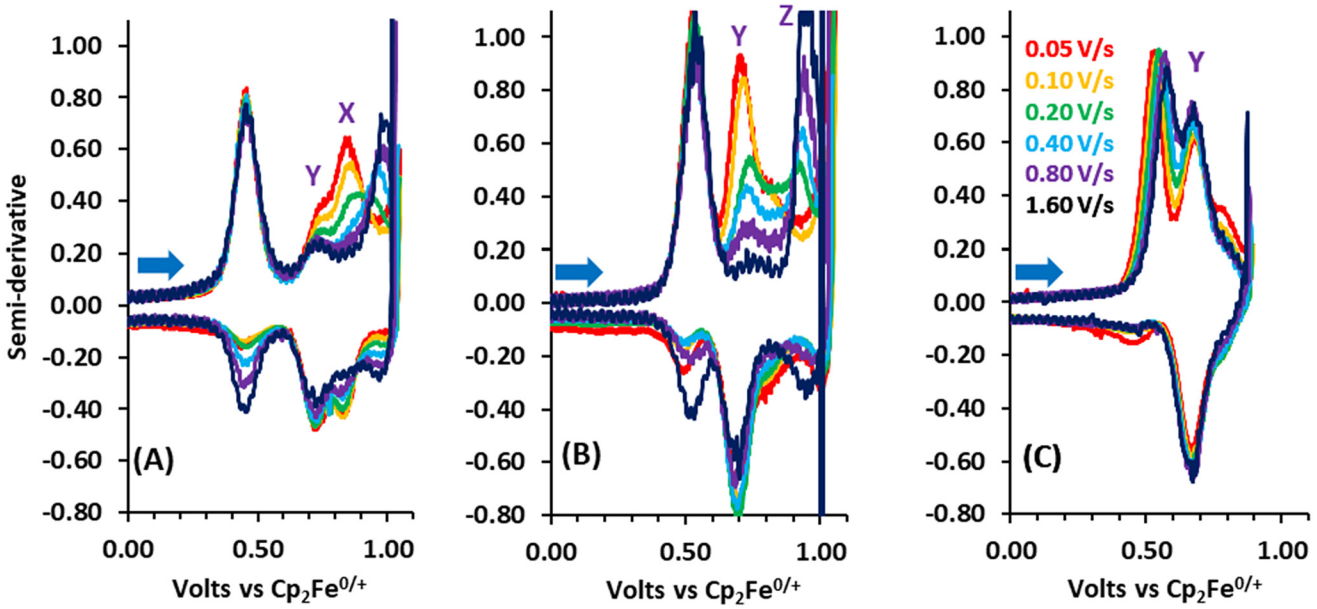

Fig. 4 Semi-derivative representation of R_u- and C_{dl}-corrected CV data collected at 298 K in CH_2Cl_2/0.1 M NBu_4PF_6 with 0.020 cm^2 Pt working electrode, C_{dl} = 1.0 μF. (A) 1.1 mM complex **1a**, R_u = 1.5 kΩ, (B) 1.3 mM complex **1b**, R_u = 1.5 kΩ, (C) 1.0 mM complex **1c**, R_u = 1.2 kΩ. Blue arrow indicates initial scan direction. See text for discussion of processes X and Y.

In contrast to **1a**, complex **2a** exhibits an irreversible oxidation at all scan rates. Oxidation of **2a** results in a reversible daughter peak which is assigned to the aquo complex [Ru(TAP)(NO)(H_2O)]$^+$. Comparison of scans for **2a** at 0.55 mM and 1.43 mM show no concentration-dependence, but they do reveal evidence for electrode fouling after a dozen scans or so at high concentrations. The slope of a plot of *iR*-corrected E_{pa} values *vs.* log(ν) is 55 mV per decade, a value which indicates a diffusion-limited follow-up reaction and therefore an exceedingly short lifetime for the **2a**$^+$ cation. This oxidation results in a reversible follow-up feature at 0.76 V *vs.* $Cp_2Fe^{0/+}$, similar to what was observed for **1a** (ESI Fig. S11A†).

The electrochemical behavior of **2b** is qualitatively similar to **1b** and can be rationalized similarly. A mechanism involving irreversible first order dissociation of the "$^{\bullet}$OAr^1" phenoxyl radical (Ar^1 = –C_6H_3-(2-NHC(=O)CF_3)) followed by rapid trapping of the coordinatively unsaturated cationic Ru-complex by adventitious ligands such as water in dichloromethane[35] is consistent with the results for both compounds *via* digital simulations (*vide infra*).

Similar to what was observed for **1c**, CV's of complex **2c** show no change in shape between scans performed at 0.6 mM and 1.0 mM and the slope of a plot of E_{pa} *vs.* log(ν) was found to be 53 mV per decade, *i.e.* the follow-up reaction appears to be diffusion-limited and therefore somewhat faster than the process for **1c** which only gave a E_{pa} *vs.* log(ν) slope of 37 V per decade.

EPR spectroelectrochemistry

Room temperature EPR spectroelectrochemistry was attempted for **1a–1c** with only **1b** yielding a detectable signal. ESI Fig. S13† displays the EPR spectroelectrochemistry data of **1b** in 1.0 M NBu_4PF_6/CH_2Cl_2 after 1 μA of anodic current was passed through the cell for 2 minutes during a chronopotentiometry experiment. The EPR spectroelectrochemistry cell is highly resistive, which poses a problem for its use with a potentiostat in controlled-potential mode. In controlled-current (galvanostatic) mode, it was found that a stable potential at the first oxidation could be applied for extended periods of time if the current was limited to 1 μA. The level of current was sufficient to oxidize **1b** without raising the applied potential above $E^{o\prime}$ = 0.44 V. *vs.* $Cp_2Fe^{0/+}$, *i.e.* the $E^{o\prime}$ value of **1b**'s first oxidation. Under these conditions, a persistent EPR signal increases in intensity over a period of over 30 minutes. Increasing the applied current to 10 μA or 100 μA allowed for more positive potentials to be applied while being measured. Application of increased current led to rapid increases in the signal intensity observed, without the appearance of any new observable signals. Kaim *et al.*[31] have investigated the [Ru(OEP)(NO)(H_2O)]$^{2+}$ π-cation radical under similar conditions using spectroelectro-EPR. They reported a *g* value for the complex of 2.0017 and a peak width of 25 Gauss. The EPR signals observed in this investigation possess a *g* value of 2.0029 with a peak width of 4.9 Gauss which are values consistent with a free organic radical, most likely the $^{\bullet}$OAr^1 phenoxyl radical. The potential applied to yield this signal is insufficient to oxidize [Ru(OEP)(NO)(H_2O)]$^+$ to its EPR-active 17-electron dicationic form.

IR spectroelectrochemistry

The fiber-optic infrared spectroelectrochemistry (IR-SEC) method probes the layer of solution adjacent to the electrode

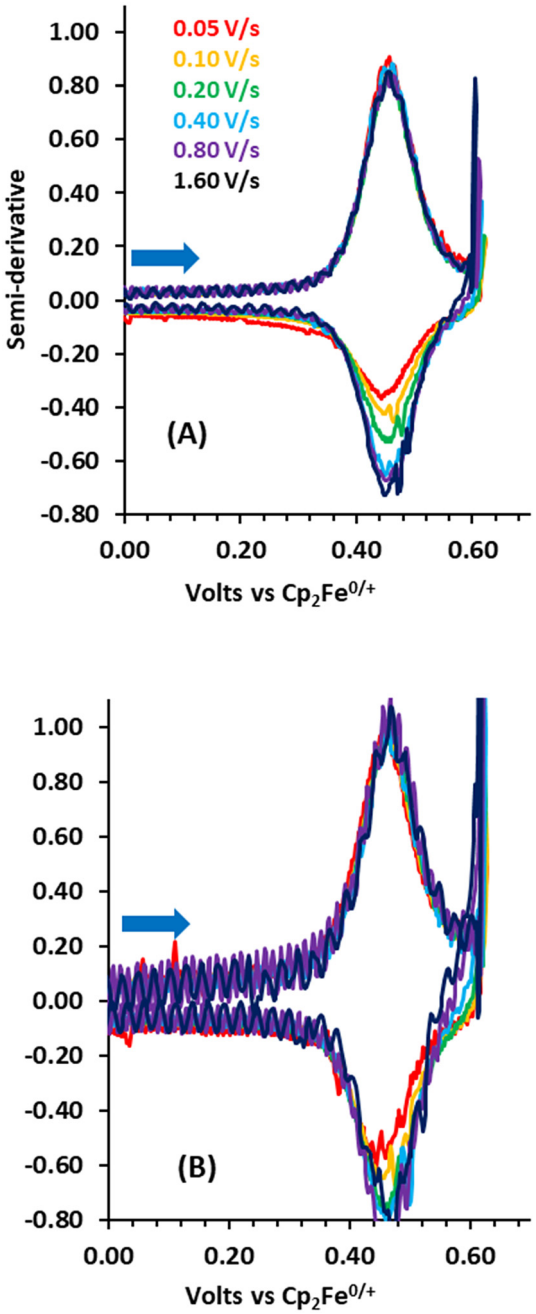

Fig. 5 Semi-derivative representation of R_u- and C_{dl}-corrected CV data collected at 298 K in CH_2Cl_2/0.1 M NBu_4PF_6 with 0.020 cm^2 Pt working electrode, R_u = 1.5 kΩ, C_{dl} = 1.0 μF. (A) 1.1 mM complex **1a**, (B) 0.27 mM complex **1a**. Blue arrow indicates initial scan direction.

(*i.e.* the diffusion layer) rather than the electrode surface. Since the IR beam approaches the electrode normal to the surface, there is a node of zero IR intensity at the surface of the electrode, so no IR radiation can be absorbed there. The data is collected over a 1 minute period when the current at the electrode has reached a near-steady state, in practice after about 10 seconds. As a result, short-lived species are not expected to be observed. At higher applied potentials, highly oxidizing species generated at the electrode are reduced by starting material from the bulk solution. Thus, signals due to mono-oxidized material are detected even when higher potentials are applied. Weak signals due to highly oxidized material at close distances to the electrode are observed as shoulders.

Table 1 Electrochemical data for **1a–1c** and **2a–2c**

Complex	$E^{o\prime}$ first oxidation process	$E^{o\prime}$ second oxidation process (aqua complex)	$E^{o\prime}$ further oxidations
1a	0.44	0.71	
1b	0.54	0.72	0.83[b], 0.96[c]
1c	0.58[a]	0.71	
2a	0.64[a]	0.76	1.06
2b	0.62	0.76	1.06
2c	0.63[a]	0.78	1.06

Potentials are reported in volts and referenced to the Fc/Fc^+ couple. [a] E_{pa} at 0.2 V s^{-1} is reported due to irreversibility. [b] Dominant at slow scan rates. [c] Dominant at fast scan rates.

The results of IR-SEC investigations for compounds **1a**, **1b** and **1c** are displayed in Fig. 6, 7 and 8 respectively as difference spectra. The data for compounds **2a**, **2b** and **2c** are very similar and are included as ESI Fig. S14, S15, and S16† respectively. The most striking similarity in the data for all complexes is the behavior of the ν_{NO} bands and the appearance of π-radical cation bands upon oxidation. The downward-pointing feature in the 1822–1857 cm^{-1} range of each spectrum results from consumption of the starting material. The decrease in the electron density at the metal center diminishes backbonding and

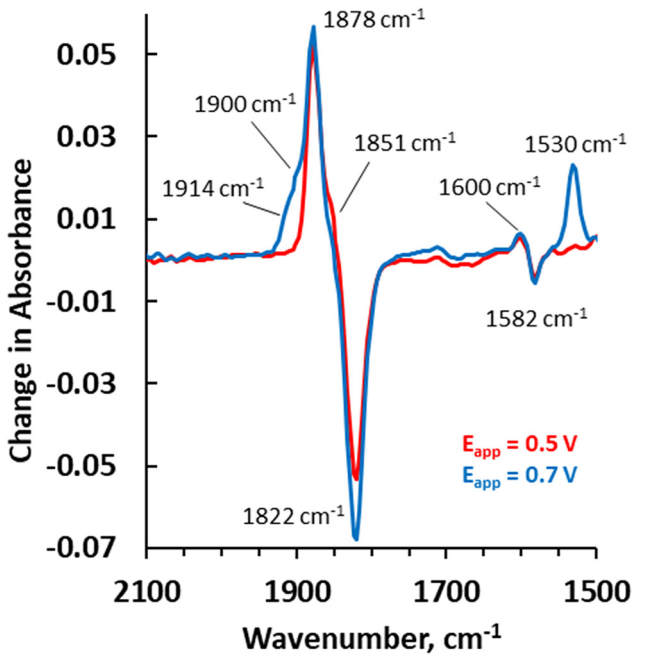

Fig. 6 Fiber-optic IR-spectroelectrochemistry of 1.1 mM **1a** in CH_2Cl_2/0.1 M NBu_4PF_6 at 298 K, 3 mm Pt working electrode. Red trace recorded at 0.5 V *vs.* $Cp_2Fe^{0/+}$, blue trace recorded at 0.7 V *vs.* $Cp_2Fe^{0/+}$, 60 s data collection.

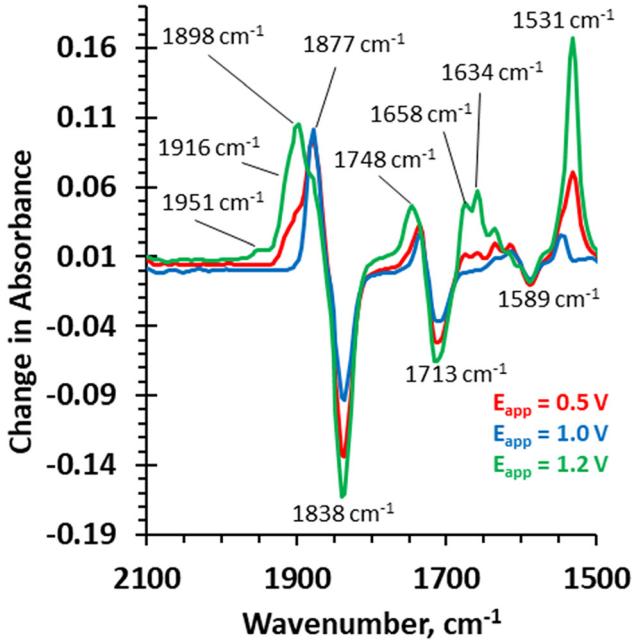

Fig. 7 IR spectroelectrochemistry of 1.4 mM **1b** in CH_2Cl_2/0.1 M NBu_4PF_6 at 298 K, 3 mm Pt working electrode. Red trace recorded at 0.5 V *vs.* $Cp_2Fe^{0/+}$, blue trace recorded at 1.0 V *vs.* $Cp_2Fe^{0/+}$, green trace recorded at 1.2 V *vs.* $Cp_2Fe^{0/+}$.

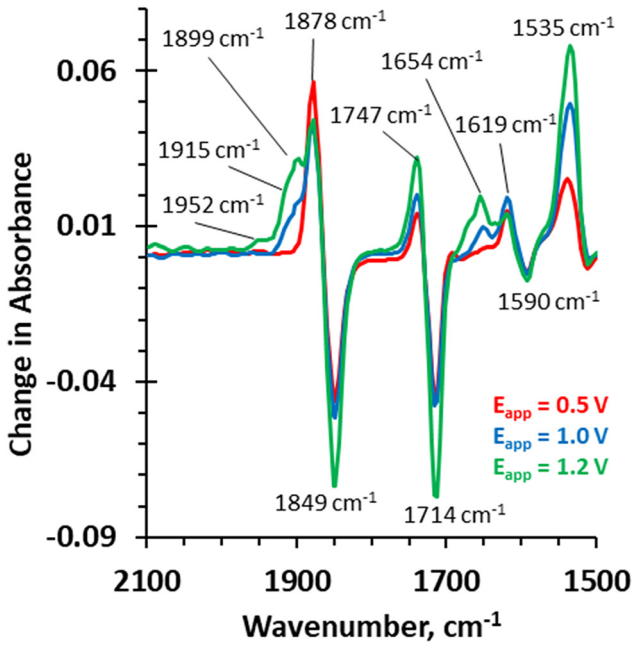

Fig. 8 IR spectroelectrochemistry of 1.0 mM **1c** in CH_2Cl_2/0.1 M NBu_4PF_6 at 298 K, 3 mm Pt working electrode. Red trace recorded at 0.5 V *vs.* $Cp_2Fe^{0/+}$, blue trace recorded at 1.0 V *vs.* $Cp_2Fe^{0/+}$, green trace recorded at 1.2 V *vs.* $Cp_2Fe^{0/+}$.

causes a shift of the NO band to higher frequency. New ν_{NO} bands due to electrode products manifest as upward-pointing features. A band at 1878 cm^{-1} is observed when IR data is recorded at an applied potential (E_{app}) of 0.5 V *vs.* $Cp_2Fe^{0/+}$ corresponding to the first oxidation for each OEP complex **1a–1c**. This band matches the ν_{NO} band previously observed for $[Ru(OEP)(NO)(H_2O)]^+$.[31] The aquo complex likely forms after loss of the phenoxy moiety as a neutral species and trapping of the Ru complex by adventitious water. The corresponding band due to $[Ru(TAP)(NO)(H_2O)]^+$ from complexes **2a–2c** occurs at 1885 cm^{-1}, and is at a slightly higher frequency consistent with the less electron-donating nature of the TAP ligand relative to OEP.

Bands at 1900, 1898, and 1899 cm^{-1} are observed for **1a**, **1b**, and **1c** respectively at applied potentials of 0.7 V *vs.* $Cp_2Fe^{0/+}$. These are assigned to $[Ru(OEP)(NO)(H_2O)]^{2+}$ which has a ν_{NO} band reported at 1895 cm^{-1} and a band reported at 1531 cm^{-1} due to it being a porphyrin π-cation.[31] Such bands are observed in the 1520–1570 cm^{-1} region for a variety of OEP porphyrin π-cation species.[36–38] Accordingly, bands 1530, 1531 and 1535 cm^{-1} observed after the first oxidation of **1a**, **1b**, and **1c** respectively are assigned to the dicationic aquo species. The ν_{NO} bands assigned to $[Ru(TAP)(NO)(H_2O)]^{2+}$ appear as poorly defined shoulders in the 1900–1921 cm^{-1} range for **2a–2c** respectively. Since TPP-type π-radical cations have IR bands in the 1270–1295 cm^{-1} region, they would be obscured by solvent/electrolyte bands in the present study.

An additional ν_{NO} band is also observed as a very small shoulder upon oxidation at 0.7 V *vs.* $Cp_2Fe^{0/+}$ at 1914, 1916, and 1915 cm^{-1} for **1a**, **1b**, and **1c** respectively. Finally, bands at 1951 and 1952 cm^{-1} are observed when **1b** and **1c** are oxidized at 1.0 V *vs.* $Cp_2Fe^{0/+}$. Again, these agree with the reported value for the $[Ru(OEP)(NO)(H_2O)]^{3+}$ complex at 1850 cm^{-1}.[31] Bands at similar positions are observed for **2a–2c**.

A very subtle difference is noted in the data for **1a**, where a shoulder is observed in the first oxidation at 1851 cm^{-1}. This band is not present when higher potentials are applied and is tentatively assigned to $\mathbf{1a}^+$. The relatively small shift in ν_{NO} (29 cm^{-1}) is consistent with oxidation at a ligand (*i.e.* the OPh group) rather than at the Ru–NO unit. This assignment is consistent with the behavior of the peak labelled X in Fig. 4.

All the phenoxide complexes show a variety of non-ν_{NO} bands in the IR-SEC results. These bands depend on the phenoxide ligand, as demonstrated in ESI Fig. S17–S19,† which show oxidations of the analogous TAP and OEP complexes overlaid *i.e.* **1a** with **2a**, **1b** with **2b** and **1c** with **2c**. Oxidation of each compound at their respective first oxidation potential results in the disappearance of bands at 1582, 1589, and 1590 cm^{-1} and the appearance of new peaks at 1600 cm^{-1}, 1619 cm^{-1}, and 1615 cm^{-1} for compounds **1a–1c** respectively. In the starting materials, these bands are assigned to the π-system of the coordinated phenoxide ligand. For **1a** and **2a**, the new peak at 1600 cm^{-1} is consistent with the presence of phenol possibly formed from the phenoxide radical by H-atom abstraction from solvent or supporting electrolyte. For **1b**, **1c**, **2b**, and **2c** the peaks at 1615–1619 cm^{-1} are similarly assigned to the phenol form of the ligands.

For **1b** and **2b**, the band observed at 1635 cm^{-1} at the first oxidation is assigned to the persistent phenoxide radical observed

by EPR for **1b** and whose lifetime is long enough that it should easily be observed by this IR-SEC method. Its peaks are consistent with those reported previously[39,40] for C_{ortho}–C_{meta} bonds in phenoxyl-based radical which exhibit semiquinoid character. Thus, the IR spectroelectrochemistry data is consistent with the phenoxyl-ligand in each complex being the observed site of net oxidation for **1b** and **2b** under our conditions.

For the first oxidation of complexes **1b** and **2b**, the IR band at 1713 cm^{-1} changes to 1735 cm^{-1} and is assigned to a ligand ν_{CO} band of the aryloxide group. Similarly, the aryloxide ν_{CO} band in **1c** and **2c** at 1714 cm^{-1} moves to 1732 cm^{-1} at the first oxidation. Not surprisingly, the bands are more prominent in the disubstituted OAr^2 complex (**1c**, **2c**) than the OAr^1 (**1b**, **2b**) complex and not observed at all for the OPh (**1a**, **2a**) derivatives. For **1c** and **2c**, oxidation at higher potentials changes the final ν_{CO} band to 1747 cm^{-1}, and a band at 1654 cm^{-1} increases in intensity. For **1b** and **2b**, the product ν_{CO} band at 1735 also moves to 1748 cm^{-1} upon oxidation at 1.2 V *vs.* $Cp_2Fe^{0/+}$. The appearance of features in the 1654–1674 cm^{-1} region at higher potentials for all these compounds likely result from further reactivity of the persistent phenoxide radicals that should form under these conditions.

Digital simulations

Digital simulations of the CV data obtained for **1a** and for the **1b** and **2b** pair were performed in detail. The concentration studies for **1a** suggest that the immediate consequence of oxidation is a rate limiting second-order (in ruthenium) follow-up reaction. This process is subsequently followed by a fast and apparently irreversible reaction with adventitious water as supported by the IR-SEC results. In contrast, the CV data and simulations for **1b** are more consistent with first-order dissociation of the aryloxyl radical $^{\bullet}OAr^1$ (observed by EPR) followed by apparently irreversible formation of the aquo complex (observed by IR-SEC).

For complex **1a**, the possibility that both types of reactions operated in competition with reversibility (with and without follow-up reactions) was considered but yields poor fits *via* digital simulation. When the follow-up reactions were modelled as irreversible better fits were obtained.

The "dimer^{2+}" species and the "Ru^+" must eventually react with adventitious water to yield an aquo complex, but this process does not seem to influence the observed rate-limiting steps. As discussed in the Conclusion section, we tentatively suggest that dimerization occurs through the coordinated OPh groups in $\mathbf{1a}^+$.

Interestingly, during the curve fitting process, the value of k_{1a} refines to 1.9×10^{-13} s^{-1}, a value too small to have an effect on the simulation results. When this data is considered as a simple EC mechanism with an irreversible second-order chemical step, curve fitting yields a value for k_{d1a} of 2.2×10^3 M^{-1} s^{-1}. The 99.7% confidence interval for this value is $(2.0–2.4) \times 10^3$ M^{-1} s^{-1}. The DigiElch results are in good agreement with a separate analysis of this data by Saveant's method for electrodimerization,[41] which gives a rate constant for k_{d1a} in the range of 1.1×10^3–2.2×10^3 M^{-1} s^{-1}. A new set of i_{pa}/i_{pc} *vs.* log(λ) values (λ = dimensionless kinetic parameter) were simulated *via* DigiElch to facilitate this analysis, (see ESI Table S2, ESI Fig. S20†). Comparison of experimental and simulated data are shown in Fig. 9 for ν = 0.20 V s^{-1} with overlays for all data shown in Fig. S21.†

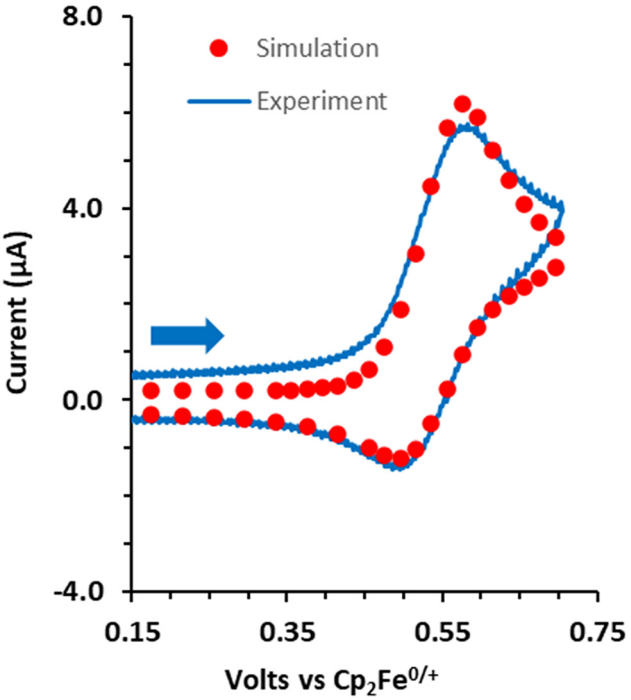

Fig. 9 Digital simulations of 1.1 mM **1a** for a second-order follow-up reaction at 200 mV s^{-1} at 298 K in CH_2Cl_2/0.1 M NBu_4PF_6. No R_u or C_{dl} correction applied to experimental data. Simulation parameters: R_u = 1.5 kΩ, C_{dl} = 1 μF, $D°$ values = 1.0×10^{-5} cm^2 s^{-1}, 0.017 cm^2 Pt electrode.

The best digital simulations of the electrochemistry of species **1b** that we could obtain are displayed in ESI Fig. S22† with an example at 0.20 V s^{-1} shown in Fig. 10. The initial strategy was to simulate the data based on a mechanism similar to Scheme 1 but where irreversible first-order and second-order reactions compete (Scheme 2).

Under these conditions, the best fit to experimental data occurs when the second-order rate constant for the follow-up reaction is too slow to be significant ($k_{d1b} = 1.01 \times 10^{-6}$ M^{-1} s^{-1}) while k_{1b} = 1.02 s^{-1}. In a separate set of simulations which included only an irreversible first-order follow-up reaction, the value of k_{1b} = 1.00 s^{-1} falls within a 99.7% confidence interval of 0.976 to 1.026 s^{-1}. In contrast to species **1a**, the digital simulations of species **1b** strongly support a first-order process which follows the initial oxidation. This process presumably involves the loss of the OAr^1 ligand as a radical as per the EPR results.

The two subsequent oxidations observed in the CV's of **1b** can also be modelled (ESI Fig. S23†). The feature simulated at $E°'$ = 0.71 V *vs.* $Cp_2Fe^{0/+}$ is more prominent at fast scan rates and is assigned to oxidation of $\mathbf{1b}^+$ to $\mathbf{1b}^{2+}$. The latter appears to irreversibly dissociate the $^{\bullet}OAr^1$ ligand at a very fast rate. The feature at $E°'$ = 1.11 V *vs.* $Cp_2Fe^{0/+}$ which is more prominent at low scan rates is consistent with oxidation of $[Ru(OEP)(NO)(H_2O)]^+$.

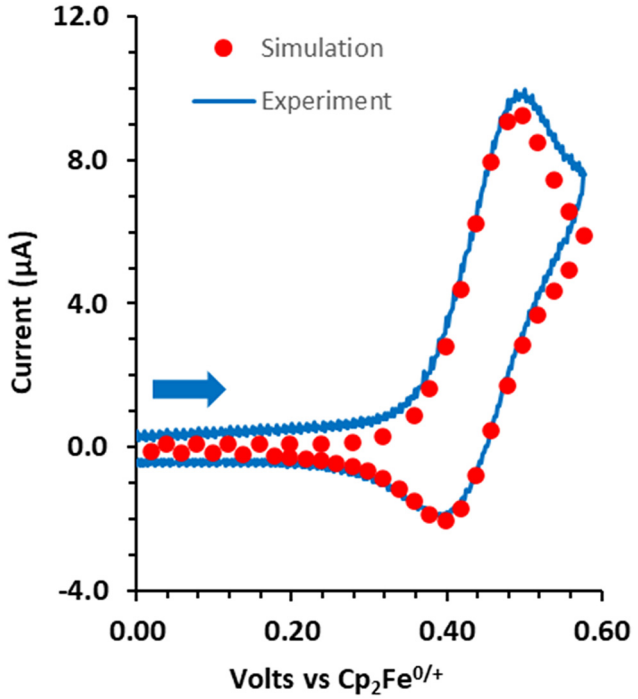

Fig. 10 Digital simulations of 1.2 mM **1b** for a second-order follow-up reaction at 200 mV s^{-1} at 298 K in CH_2Cl_2/0.1 M NBu_4PF_6. No R_u or C_{dl} correction applied to experimental data. Simulation parameters: R_u = 1.5 kΩ, C_{dl} = 1 μF, $D°$ values = 1.0 × 10^{-5} cm^2 s^{-1}, 0.017 cm^2 Pt electrode.

$$\begin{aligned} \mathrm{RuOPh^+ + e^- \leftrightarrows RuOPh} &\qquad E°'(\mathbf{1a}) \\ \mathrm{2\ RuOPh^+ \rightarrow \text{“}dimer^{2+}\text{”}} &\qquad k_{d1a} \\ \mathrm{RuOPh^+ \rightarrow Ru^+ + {\bullet}OPh} &\qquad k_{1a} \end{aligned}$$

Scheme 1 Competing first and second order EC reactions following the oxidation of **1a**. $E°'$ (**1a**) is the oxidation potential of **1a**, k_{d1a} is the forward rate constant for the dimer formation, and k_{1a} is the forward rate constant for phenoxyl dissociation.

$$\begin{aligned} \mathrm{(RuOAr^1)^+ + e^- \leftrightarrows RuOAr^1} &\qquad E°'(\mathbf{1b}) \\ \mathrm{2\ (RuOAr^1)^+ \rightarrow dimer^{2+}} &\qquad k_{d1b} \\ \mathrm{(RuOAr^1)^+ \rightarrow Ru^+ + {\bullet}OAr^1} &\qquad k_{1b} \end{aligned}$$

Scheme 2 Competing first and second order EC reactions. $E°'$(**1b**) is the oxidation potential of **1b**, k_{d1b} is the forward rate constant for the dimer formation, and k_{1b} is the forward rate constant for phenoxyl dissociation.

A similar analysis of **2b** yielded a first-order rate constant of k_{2b} = 0.85 s^{-1} for its follow-up reaction (see ESI Fig. S24†). Digital simulations for **1c**, **2a** or **2c** were not carried out because their first oxidation was irreversible at the scan rates used. For **1c**, the slope of 37 mV per decade from the E_{pa} *vs.* log(ν) plot suggests a minimum rate of ~10^5 s^{-1}, assuming a first order follow up reaction.[34]

Conclusions

One-electron oxidation of all compounds studied generates a cationic complex whose behavior depends on the phenoxyl structure and the porphyrin. In the presence of adventitious water, the ultimate fate of the Ru(por)(NO)moiety is to form $[Ru(por)(NO)(H_2O)]^{+/2+/3+}$, depending on the applied potential. The phenoxyl radicals appear to return to the phenol state as indicated by the spectroelectrochemistry results, most likely by reaction with the medium. This assignment seems reasonable as the rate of H-atom abstraction from tetrabutylammonium cations by $^{\bullet}$OH has been measured at 4.9 × 10^9 M^{-1} s^{-1} in aqueous solution by pulse radiolysis,[42] and H-atom abstraction from dichloromethane by $^{\bullet}$OH has been measured in the gas phase to be 1.2 × 10^{12} M^{-1} s^{-1}, and these studies were conducted over tens of seconds. H-atom abstraction is more likely than radical dimerization given the low concentration of the complexes. Interestingly, we have no observation to indicate that deprotonation of the trifluoroacetamide groups in the aryloxide ligands plays a role in the observed chemistry.

The differences observed between the OEP compounds **1a**–**1c** and the TAP compounds **2b** and **2c** can be rationalized as a result of increasing phenoxyl radical stability in the order $^{\bullet}$OPh < $^{\bullet}$OAr^1 < $^{\bullet}$OAr^2. This order of stabilities is consistent with the increasing number of resonance structures, increasing steric protection of the O-atom at the 2 and 5 positions of the phenyl ring, and the electron-withdrawing effects of the trifluoroacetamide groups. This explanation suggests the reactive $^{\bullet}$OPh radical is a poor leaving group and tends to stay within the coordination sphere in **1a**, while the $^{\bullet}$OAr^1 and $^{\bullet}$OAr^2 radicals leave the coordination sphere of the metal atom progressively faster in **1b**/**2b** and **1c**/**2c** respectively.

Two results involving **1a** and **2a** add nuance to this explanation. Firstly, **1a**$^+$ undergoes an unexpected second-order reaction in the ruthenium complex in contrast to the first order dissociation experienced by **1b**$^+$. Secondly, while TAP complexes **2b** and **2c** behave similarly to their OEP analogues **1b** and **1c**, complex **2a**$^+$ undergoes an exceedingly fast reaction in contrast to the slow reaction experienced by **1a**$^+$. These results can be rationalized by considering the different steric environments afforded by the OEP and TAP ligands. On average, the eight ethyl groups in OEP can protect the OPh ligand in **1a**$^+$ from solvent and supporting electrolyte more effectively than the four phenyl groups in the TAP complex **2a**$^+$, leading to the latter's dramatically reduced lifetime. The longer lifetime of the **1a**$^+$ cation permits slow reactions such as dimerization. The dimerization of phenoxyl radicals have been studied.[43] Diketones form in these reactions and then tautomerize into dihydroxybiphenyls. If **1a**$^+$ reacts by dimerization through the phenoxide ligand, the weakly bound ketone intermediate would later be displaced by adventitious water. The displaced ketone would then isomerize into 4,4′-dihydroxybiphenyl whose known IR spectrum[44] is consistent with the IR bands observed in the spectroelectrochemistry of **1a**.

These results underline how systematic variation in structure can lead to a surprising variety of consequences in the reactions which follow electron transfer.

Author contributions

The manuscript as written through the contributions of all authors. All authors have approved the final version of the manuscript.

Data availability

Crystallographic data for **2b** and **2c** have been deposited at the CCDC as structures 2340852 and 2340853 respectively. Other data supporting this article have been included as part of the ESI.†

Conflicts of interest

The authors declare no competing interests.

Acknowledgements

We are grateful to the U.S. National Science Foundation (NSF) for support for GBR-A and MJS (CHE-2154603, CHE-1900181, CHE-1566509). This material is based in part upon work supported by (while GBR-A was serving at) the NSF.

References

1 C. D. Putnam, A. S. Arvai, Y. Bourne and J. A. Tainer, Active and inhibited human catalase structures: ligand and NADPH binding and catalytic mechanism. Edited by R. Huber, *J. Mol. Biol.*, 2000, **296**(1), 295–309.

2 M. Alfonso-Prieto, X. Biarnés, P. Vidossich and C. Rovira, The Molecular Mechanism of the Catalase Reaction, *J. Am. Chem. Soc.*, 2009, **131**(33), 11751–11761.

3 P. Nicholls, I. Fita and P. C. Loewen, *Adv. Inorg. Chem.*, 2001, **51**, 51–106.

4 D. Clark, J. Durner, D. A. Navarre and D. F. Klessig, Nitric Oxide Inhibition of Tobacco Catalase and Ascorbate Peroxidase, *Mol. Plant-Microbe Interact.*, 2000, **13**(12), 1380–1384.

5 L. Cheng and G. B. Richter-Addo, The Binding and Activation of Nitric Oxide by Metalloporphyrins and Heme, in *The Porphyrin Handbook, Vol. 4 (Biochemistry and Binding: Activation of Small Molecules)*, ed. R. Guilard, K. Smith and K. M. Kadish, Academic Press, New York, 2000, pp. 219–291.

6 N. Lehnert, E. Kim, H. T. Dong, J. B. Harland, A. P. Hunt, E. C. Manickas, K. M. Oakley, J. Pham, G. C. Reed and V. S. Alfaro, The Biologically Relevant Coordination Chemistry of Iron and Nitric Oxide: Electronic Structure and Reactivity, *Chem. Rev.*, 2021, **121**, 14682–14905.

7 G. C. Brown, Reversible Binding and Inhibition of Catalase by Nitric Oxide, *Eur. J. Biochem.*, 1995, **232**(1), 188–191.

8 R. L. Khade, E. G. Abucayon, D. R. Powell, G. B. Richter-Addo and Y. Zhang, Insights into the Observed *trans*-Bond Length Variations upon NO Binding to Ferric and Ferrous Porphyrins with Neutral Axial Ligands, *ACS Omega*, 2021, **6**, 24777–24787.

9 N. Xu, L. E. Goodrich, N. Lehnert, D. R. Powell and G. B. Richter-Addo, Preparation of the Elusive [(por)Fe(NO)(O-ligand)] Complex by Diffusion of Nitric Oxide into a Crystal of the Precursor, *Angew. Chem., Int. Ed.*, 2013, **52**(14), 3896–3900.

10 D. Awasabisah, N. Xu, K. P. Sharmah Gautam, D. R. Powell, M. J. Shaw and G. B. Richter-Addo, Stable ruthenium nitrosyl porphyrins with axial O-bonded ligands; preparation and redox behavior, *Dalton Trans.*, 2013, **42**(24), 8537–8540.

11 D. Awasabisah, N. Xu, K. P. S. Gautam, D. R. Powell, M. J. Shaw and G. B. Richter-Addo, Preparation, Characterization, Electrochemistry, and Infrared Spectroelectrochemistry of Ruthenium-Nitrosyl Porphyrins Containing η^1-O-Bonded Axial Carboxylates, *Eur. J. Inorg. Chem.*, 2016, **2016**(4), 509–518.

12 D. Kanamori, Y. Yamada, A. Onoda, T. Okamura, S. Adachi, H. Yamamoto and N. Ueyama, Structures and Properties of Octaethylporphinato(phenolate)iron(III) Complexes with NH···O Hydrogen Bonds: Modulation of Fe-O Bond Character by the Hydrogen Bond, *Inorg. Chim. Acta*, 2005, **358**, 331–338.

13 N. Ueyama, N. Nishikawa, Y. Yamada, T. Okamura, S. Oka and A. Nakamura, Synthesis and Properties of Octaethylporphinato(arenethiolato)iron(III) Complexes with Intramolecular NH···S Hydrogen Bond: Chemical Function of the Hydrogen Bond, *Inorg. Chem.*, 1998, **37**, 2415–2421.

14 (*a*) A. J. Warhausen, J. R. Zink, B. J. Ross, A. R. Ramuglia, J. Londono-Salazar, D. R. Powell, M. J. Shaw and G. B. Richter-Addo, Ruthenium nitrosyl porphyrins coordinated with aryloxides containing internal hydrogen bonds, *Eur. J. Inorg. Chem.*, 2024, DOI: 10.1002/ejic.202400648; (*b*) A. Warhausen, *Synthesis, Characterization, Electrochemistry, and Spectroelectrochemistry of (por)Ru(NO)(OR) (por = TPP and OEP, R = -C_6H_3-2,6-NHC(=O)CF_3, -C_6H_4-2-NHC(=O)CF_3 and –Ph) Complexes*, University of Oklahoma, 2012.

15 J. Zink, *Synthesis and redox behavior of ruthenium nitrosyl porphyrin complexes*, University of Oklahoma, 2022.

16 M. J. Shaw, R. L. Henson, S. E. Houk, J. W. Westhoff, G. B. Richter-Addo and M. W. Jones, Fiber-Optic IR Reflectance Spectroelectrochemistry: Isomerization of a Manganese Pyranyl Complex, *J. Electroanal. Chem.*, 2002, **534**, 47–53.

17 J. R. Zink, E. G. Abucayon, A. R. Ramuglia, A. Fadamin, J. E. Eilers, G. B. Richter-Addo and M. J. Shaw, Electrochemical Investigation of the Kinetics of Chloride Substitution upon Reduction of [Ru(porphyrin)(NO)Cl] Complexes in Tetrahydrofuran, *ChemElectroChem*, 2018, **5**(6), 861–871.

18 D. Garreau and J. Savéant, Linear sweep voltammetry—Bandpass limitations and maximum usable sweep rate in the study of faradaic processes, *J. Electroanal. Chem. Interfacial Electrochem.*, 1974, **50**, 1–22.

19 (*a*) J. E. B. Randles, *Trans. Faraday Soc.*, 1948, **44**, 327; (*b*) A. Sevcik, *Collect. Czech. Chem. Commun.*, 1948, **13**, 349;

(*c*) H. Matsude and Y. Z. Ayabe, *Electrochemistry*, 1955, **59**, 494.

20 J.-M. Saveant, *Elements of Molecular and Biomolecular Electrochemistry: An Electrochemical Approach to Electron Transfer Chemistry*, John Wiley & Sons, Inc, Hoboken, New Jersey, 2006.

21 A. Molina and I. Morales, Comparison Between Derivative and Differential Pulse Voltammetric Curves of EC, CE and Catalytic Processes at Spherical Electrodes and Microelectrodes, *Int. J. Electrochem. Sci.*, 2007, **2**, 386–405.

22 P. J. Mahon and K. B. Oldham, Voltammetric Modelling via extended semiintegrals, *J. Electroanal. Chem.*, 1998, **445**, 179–195.

23 (*a*) P. J. Mahon and K. B. Oldham, Semioperations and Convolutions in Voltammetry, *ChemElectroChem*, 2018, **5**, 839–848; (*b*) J. M. Saveant and D. Tessier, Convolution potential sweep voltammetry. IV. Homogeneous follow-up chemical reactions, *J. Electroanal. Chem.*, 1975, **61**, 251.

24 R. Klicka, Adsorption in semi-differential voltammetry, *J. Electroanal. Chem.*, 1998, **455**, 253–257.

25 J. A. Johnson, N. T. Rodeberg and R. M. Wightman, Measurement of Basal Neurotransmitter Levels Using Convolution-Based Nonfaradaic Current Removal, *Anal. Chem.*, 2018, **90**(12), 7181–7189.

26 P. Dalrymple-Alford, M. Goto and K. B. Oldham, Shapes of derivative neopolarograms, *J. Electroanal. Chem. Interfacial Electrochem.*, 1977, **85**, 1–15.

27 M. H. Rahman, A. Atifi, J. Rosenthal and M. D. Ryan, Reversible Proton-Coupled Reduction of an Iron Nitrosyl Porphyrin within $[DBU–H]^+$-Based Protic Ionic Liquid Nanodomains, *Inorg. Chem.*, 2021, **60**, 10631–10641.

28 S. S. Eaton and G. R. Eaton, Rotation of Phenyl Rings in Metal Complexes of Substituted Tetraphenylporphyrins, *J. Am. Chem. Soc.*, 1975, **97**, 3660–3666.

29 S. S. Eaton and G. R. Eaton, Effects of Para Substituent and Metal Ion on Rates of Phenyl Ring Rotation in Ruthenium, Indium, and Titanium Complexes of Para-Substituted Tetraphenylpophyrins, *J. Am. Chem. Soc.*, 1977, 6594–6599.

30 C. P. Andrieux, G. Delgado, J. M. Saveant and K. B. Su, Improvement and estimation of precision in the cyclic voltammetric determination of rate constants and activation parameters of coupled homogeneous second order reactions. Reaction of n-butyl bromide with anthracene anion radicals, *J. Electroanal. Chem.*, 1993, **348**, 141–154.

31 P. Singh, A. K. Das, B. Sarkar, M. Niemeyer, F. Roncaroli, J. A. Olabe, J. Fiedler, S. Záliš and W. Kaim, Redox Properties of Ruthenium Nitrosyl Porphyrin Complexes with Different Axial Ligation: Structural, Spectroelectrochemical (IR, UV–Visible, and EPR), and Theoretical Studies, *Inorg. Chem.*, 2008, **47**, 7106–7113.

32 C. P. Andrieux, A. Le Gorande and J.-M. Saveant, *J. Am. Chem. Soc.*, 1982, **114**, 6892.

33 (*a*) D. J. Kuchynka, C. Amatore and J. K. Kochi, Manganese (0) radicals and the reduction of cationic carbonyl complexes: selectivity in the ligand dissociation from 19-electron species, *Inorg. Chem.*, 1986, **25**, 4087–4097; (*b*) C. Amatore, P. J. Krusic, S. U. Pedersen and J.-N. Verpeaux, Rate and Mechanism of the Reductions of Iron Pentacarbonyl and Chromium Hexacarbonyl to Their Metalate Complexes, *Organometallics*, 1995, **14**, 640–649.

34 C. Amatore, P. J. Krusic, S. U. Pedersen and J.-N. Verpeaux, Rate and Mechanism of the Reductions of Iron Pentacarbonyl and Chromium Hexacarbonyl to Their Metalate Complexes, *Organometallics*, 1995, **14**(2), 640–649.

35 P. Di Profio, R. Germani, G. Onori, A. Santucci, G. Savelli and C. A. Bunton, Relation between the Infrared Spectrum of Water and Decarboxylation Kinetics in Cetyltrimethylammonium Bromide in Dichloromethane, *Langmuir*, 1998, **14**, 768–772.

36 E. T. Shimomura, M. A. Phillippi, H. M. Goff, W. F. Scholz and C. A. Reed, Infrared Spectroscopy of Oxidized Metalloporphyrins: Detection of a Band Diagnostic of Porphyrin-Centered Oxidation, *J. Am. Chem. Soc.*, 1981, **103**, 6778–6780.

37 N. Xu, J. Lilly, D. R. Powell and G. B. Richter-Addo, Synthesis, Characterization, and Infrared Reflectance Spectroelectrochemistry of Organoruthenium Nitrosyl Porphyrins, *Organometallics*, 2012, **31**(3), 827–834.

38 D. H. Jones and A. S. Hinman, *In situ* infrared spectroelectrochemical studies of tetraphenylporphyrin complexes containing manganese, iron and cobalt, *J. Chem. Soc., Dalton Trans.*, 1992, (9), 1503–1508.

39 R. Schnepf, A. Sokolowski, J. Müller, V. Bachler, K. Wieghardt and P. Hildebrandt, Resonance Raman Spectroscopic Study of Phenoxyl Radical Complexes, *J. Am. Chem. Soc.*, 1998, **120**(10), 2352–2364.

40 J. Spanget-Larsen, M. Gil, A. Gorski, D. M. Blake, J. Waluk and J. G. Radziszewski, Vibrations of the Phenoxyl Radical, *J. Am. Chem. Soc.*, 2001, **123**(45), 11253–11261.

41 C. P. Andrieux and J.-M. Saveant, Electrodimerization 1. One-electron irreversible dimerization, diagnostic criteria, and rate determination procedures for voltammetric studies, *J. Electroanal. Chem. Interfacial Electrochem.*, 1970, **26**, 147–186.

42 K. Bobrowski, Pulse radiolysis studies concerning the reactions of hydrogen abstraction from tetraalkylammonium cations, *J. Phys. Chem.*, 1980, **84**, 3524–3529.

43 L. R. Mahoney and S. A. Weiner, Mechanistic study of the dimerization of phenoxyl radicals, *J. Am. Chem. Soc.*, 1972, **94**, 585–590.

44 The IR spectrum of 4,4′-dihydroxybiphenyl is available at **https://webbook.nist.gov/cgi/inchi/InChI%3D1S/C12H10O2/c13-11-5-1-9(2-6-11)10-3-7-12(14)8-4-10/h1-8%2C13-14H**, last accessed 04/28/2024.